

Probing the Surface of $\text{La}_{0.6}\text{Sr}_{0.4}\text{MnO}_3$ in Water Vapor by *In Situ* Photon-In / Photon-Out Spectroscopy

Philipp Busse^{1,2,4}, Zhong Yin^{1,2,†}, Daniel Mierwaldt⁴, Julius Scholz⁴, Birte Kressdorf⁴, Leif Glaser², Piter S. Miedema², André Rothkirch², Jens Viefhaus^{2,††}, Christian Jooss^{4,5,}, Simone Techert^{1,2,3,*}, and Marcel Risch^{4,6,*}*

¹Structural Dynamics of (Bio)chemical Systems, Max-Planck-Institute for Biophysical Chemistry Göttingen, 37077 Germany

²Photon Science, Deutsches Elektronen-Synchrotron DESY, Hamburg, 22607 Germany

³Institute of X-ray Physics, University of Göttingen, 37077 Germany

⁴Institute of Materials Physics, University of Göttingen, 37077 Germany

⁵International Center for Advanced Energy Studies, University of Göttingen, Tammannstr. 4, 37077 Göttingen, Germany

⁶Helmholtz-Zentrum Berlin für Materialien und Energie GmbH, Nachwuchsgruppe Gestaltung des Sauerstoffentwicklungsmechanismus, 14109 Berlin, Germany

ABSTRACT

Resonant inelastic X-ray scattering (RIXS) is a promising method for elucidating detailed electronic structure of materials in a broad range of chemical and physical applications. Here, we use the fine fluorescence energy resolution of a RIXS spectrometer to obtain various proxies of the Mn-L edge X-ray absorption spectra (XAS) of the perovskite $\text{La}_{0.6}\text{Sr}_{0.4}\text{MnO}_3$ (LSMO) as a model catalyst for the oxygen evolution reaction (OER) and evaluate the suitability for *in situ* surface studies of this electrocatalyst. We conclude that the inverse partial fluorescence yield (IPFY) of the O 2p-1s transition and the partial fluorescence yield of the 3s-2p transition (3s-PFY) are most suitable for determining changes at the surface of the perovskite, because distortions at grazing incidence measurements are low. In particular, the negligible angular dependence of the 3s-PFY spectra can be perfectly simulated using a fluorescence model in the thin sample limit which is justified by low reabsorption of 3s-photons. Remarkably, the 3s-PFY reveals an influence of water vapor on the electronic reconstruction of the LSMO surface. Thus, our work paves the road for quantitative distortion-free X-ray spectroscopy of transition metal oxide surfaces under *in situ* conditions, which is needed to understand fundamental chemical processes such as corrosion and catalysis.

INTRODUCTION

For multistep surface reactions, as in heterogeneous catalysis, it is important to determine the active states of the surface under *operando* conditions in order to firstly determine a fundamental understanding of reaction mechanisms and to secondly use these insights to enhance the efficiency of the reaction. Therefore, *in situ* monitoring of the electronic states that are involved in the reaction is an essential step towards *operando* conditions. X-ray absorption spectroscopy (XAS) is a powerful tool for probing these states.¹ However, the photon attenuation length at the Mn-L edge (640 eV) in LSMO is about 230 nm based on the Henke tables.² In a transmission experiment, the majority of the information originates from the bulk of thin films with thicknesses less than 100 nm such as those used commonly for electrocatalysis.³⁻⁵ Thus, conventional soft XAS is not capable of distinctly observing surface processes. The dependence on film thickness and transmissivity is usually avoided by using indirect XAS methods based on spectroscopy of emitted characteristic X-rays generated by relaxation processes after core-excitation. The fluorescence radiation is a result of the filling of the generated core holes by transitions of electrons from the valence band or shells of lower energy. Mapping the X-ray emission spectra (XES) as a function of the incident energy around an absorption edge represents the so-called resonant inelastic X-ray spectroscopy (RIXS) method, a photon-in/photon-out technique (PI/PO).^{6,7} It is a powerful spectroscopic tool for the study of materials due to the two-dimensional data maps and the high resolution in the energy transfer.⁸

Using RIXS for surface sensitive studies poses a number of great challenges. The most severe one is that the suitable grazing incidence geometry for surface sensitive measurements provides only access to the surface by acquiring the emitted fluorescence spectrum. However, this usually represents only a rough proxy of an actual X-ray absorption spectrum and shows severe distortions.⁹ This also applies for total electron yield (TEY) measurements. They are

more surface sensitive due to the small escape depth of electrons of a few nanometers.¹⁰ However, application to *in situ* catalysis experiments is a challenge as they are performed through a liquid layer on top of the catalyst surface, which requires sophisticated control of the layer thickness, e.g. by dip and pull techniques.¹¹ Consequently, distortion-free fluorescence yield (FY) techniques at grazing incidence configurations are highly desirable for surface sensitive studies during *in situ* conditions.

For this study, we have chosen epitaxial (001) oriented $\text{La}_{0.6}\text{Sr}_{0.4}\text{MnO}_3$ (LSMO) thin films, because LSMO is a promising model catalyst for the oxygen evolution reaction (OER) showing activities close to IrO_2 (110) and a high structural stability.^{5,12} For surface reactivity and catalysis, the Mn 3d–O 2p states from the valence band are most relevant, since they constitute the bonding and antibonding states between Mn and O atoms in the lattice. Moreover, they are involved in changes due to bonding of water and reaction intermediates at the LSMO surface. Our study thus focuses on the Mn-L absorption edge and the related Mn 3d, 3s and O 2p fluorescence channels, which require an energy-resolving detector with high resolution as provided by the RIXS setup (Fig. 1).

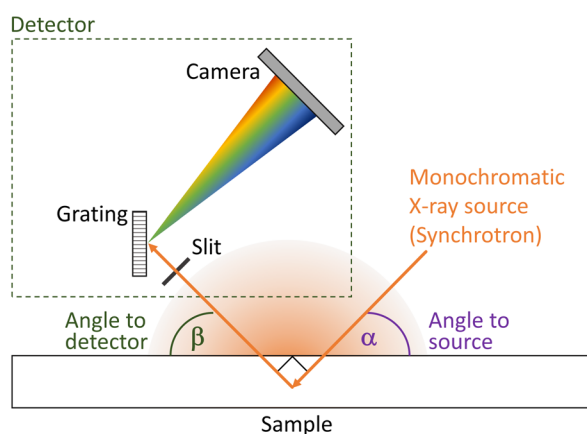


Figure 1. Schematic of the used RIXS setup (not to scale). The beam divergence of synchrotron radiation is low and was neglected. The effective divergence to the detector is given by the entrance slit (i.e. the solid angle of the detector). Further detail may be found in the text.

Decreasing the angle of incidence α to achieve surface-sensitivity, the photon penetration depth decreases with $\sin(\alpha)$, where α is defined relative to the tangent plane of the surface (Fig. 1). At a grazing incidence angle of $\alpha = 1^\circ$, the penetration depth calculated from the Henke tables² is only 4 nm or 10 unit cells of LSMO.¹³ The total fluorescence yield (TFY) and the 3d-partial fluorescence yield (3d-PFY) are the most common techniques for indirect XAS.^{14,15} The TFY is a measure of the entire induced fluorescence under excitation (as accessible by the used detector), while the 3d-PFY only records the $L\alpha/\beta$ -emission lines of the 3d-2p transition. However, the TFY and the 3d-PFY both suffer from distortions due to energy-dependent reabsorption and background effects.^{16,17} The inverse partial fluorescence yield (IPFY), which probes a non-resonant, energetically lower lying state (here: O 1s), may not only stem from the oxygen of the sample but also from oxygen of the water layer during *in situ* measurements. Thus, all three techniques may not yield undistorted *in situ* XAS spectra and must be carefully evaluated. In contrast, the 3s-PFY is hardly distorted by reabsorption as theoretically predicted by Miedema et al.¹⁸ and experimentally shown for solutions by Golnak et al.¹⁹ The main reasons are its small FY due to the small concentration of 3s holes and negligible reabsorption. In addition, the 3s-PFY exhibits a reduced energy dispersion of the emitted photons. Since the Mn 3s state is around 60 eV below the Mn 3d – O 2p valence band, it has a more localized Mn character. However, it is influenced by changes in the valence band and thus can provide information about surface bonding due to exchange and charge transfer coupling between Mn 3s holes and Mn 3d states.²⁰ Nevertheless, it has not been exploited to study surface processes under ambient conditions, in particular the interaction between an oxide surface and water vapor. A deeper understanding of this interface is crucial for catalysis of numerous reactions.

EXPERIMENTAL DETAILS

Epitaxial (001) LSMO thin film electrodes were prepared by ion-beam sputtering (IBS). 0.5 wt% Nb-doped SrTiO₃ (STNO) (CrysTec GmbH) were used as substrates. The films were deposited at 750 °C in an oxygen atmosphere of 1.8×10^{-4} mbar. The prepared films were kept under preparation conditions for 1 h and carefully cooled down to room temperature, including a resting point of 30 min at 500 °C to minimize the number of preparation-induced defects. The film thickness was 80 nm and confirmed by X-ray reflectometry (XRR). These films are single crystalline showing atomically flat surfaces, where terraces are separated by unit cell height steps. The films are uniform in structure and chemical composition. More details can be found in ref. 5.

The RIXS data was recorded at the soft X-ray beamline P04 at PETRA III, DESY in Hamburg, Germany. The beamline provides up to 10^{12} photons/s with a beamline energy resolution of <40 meV at the designated energy range of 630 to 670 eV of the Mn-L edge. The incident X-ray beam had a spot size of $10 \times 250 \mu\text{m}^2$ on the sample²¹ and possessed circular polarization. The experiment has been performed using the ChemRIXS endstation, which is a mobile endstation dedicated for RIXS experiments at the PETRA-III synchrotron and FLASH X-ray Free Electron Laser facility.^{22,23} Four LSMO samples were clamped onto the x-y-z manipulator of the ChemRIXS target chamber. All measurements discussed here were taken on the same sample. The energy-resolved fluorescence of the LSMO sample was recorded via a VLS grating and a 2D X-ray CCD (ANDOR iKon-M with 1024×1024 pixels and pixel sizes of $13 \times 13 \mu\text{m}^2$).²² This provides a combined energy resolution of around 970 meV at the Mn-L edge measured after the monochromator and spectrometer. A schematic of the experimental setup is shown in Fig. 1. The sample was mounted under a glancing angle of $\alpha = 45^\circ$ and under $\alpha = 1^\circ$ (grazing incidence). The angle between the X-ray source and detector was fixed at $\alpha + \beta = 90^\circ$ (β : angle of detection, with respect to the surface). The error

of α and β was determined to $\sigma_{\alpha,\beta} = \pm 1^\circ$. This changes the X-ray penetration depth normal to the surface by a factor of ≈ 20 from the entire film thickness down to about 4 nm, i.e. 10 unit cells. Measurements were either performed in vacuum or water vapor provided by a gas needle connected to a bottle of milliQ water.

RIXS data can be presented as a map of X-ray emission spectra as a function of incident X-ray energy. In a first step, the RIXS maps were created. The images of the CCD-detector, each presenting one emission spectrum, were first corrected for the background and freed of cosmic rays as well as of other artifacts. They were then rotated by 18.24° to align the monitored emission lines parallel to the x-axis. These images were then integrated normal to the dispersive axis in order to obtain an emission spectrum at each incident energy. According to the PI/PO approach, the emission spectra were recorded in steps of 0.2 eV of incident energy and arranged to complete RIXS maps by ordering color coded XES plots along the incident energy. Energetically, the emission axes of the RIXS maps were calibrated by measuring the elastic scattering signal at different excitation energies between 500 and 680 eV, which resulted in a calibration curve that relates the detector pixel number to emission energy. The RIXS maps acquired for the same experimental conditions were then weighted by their signal-to-noise ratio and summed up to reduce the noise level. A constant mean background was afterwards subtracted from such maps. To achieve the PFY spectra, these RIXS maps were again integrated along the axis of emission energy in an energy window given by the full width at half maximum (FWHM) of the XES generated by integration over all excitation energies at the specific transitions and represented over the axis of incident energy. For the Σ -PFY, the emission intensities of all three PFY regions have been summed up. The experimental and simulated Σ -PFY, 3d-PFY and 3s-PFY spectra were normalized via subtraction of the average between 634 and 638 eV, followed by division of the average between 658 and 670 eV (665 eV for Σ -PFY). The IPFY spectra were normalized by

subtraction of the average between 635 and 638 eV as well as division by the average between 658 and 665 eV. The energy ranges for normalization were different to reduce the influence of spectral noise on the normalization procedure. An alternative normalization using subtraction and division of linear functions was explored for the simulated IPFY because the background signal before and after the edge is not constant (Fig. S1).

THEORETICAL BASIS AND SIMULATIONS

Theoretical Background of the Fluorescence Yields

The processes of absorption and fluorescence for the excitation of LSMO at the Mn-L edge are visualized in Fig. 2. From bottom to top, different electron orbitals are shown for LSMO, either as sharp lines (Mn 2p and O 1s) or as (slightly) dispersed bands (Mn 3s, Mn 3d/O 2p). Due to the hybridization of Mn 3d and O 2p states these orbitals are represented as one band, filled up to the Fermi energy (E_F). The possible excitations at the Mn-L edge are shown on the left side (Fig. 2a). The possible decay channels of electrons into the created core holes which can generate fluorescence are shown on the right (Fig. 2b-e).

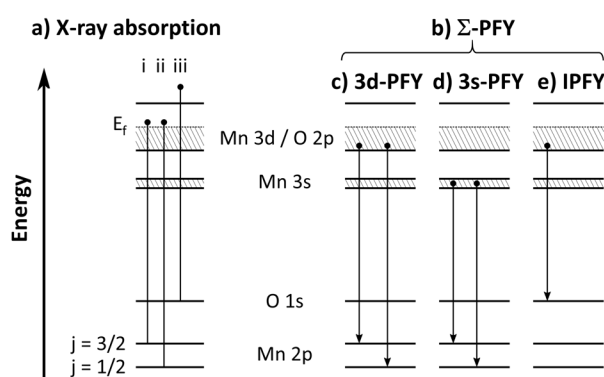


Figure 2. (a) Scheme of resonant X-ray absorption (XA) processes at (i) the Mn-L₃ and (ii) the Mn-L₂ edges, where a 2p core electron is excited to an unoccupied 3d orbital. Also shown is (iii) a non-resonant absorption process at the O-K edge where an electron in a 1s state is excited to an unbound state, i.e. vacuum. (b) Illustration of various decay channels contributing to the total fluorescence yield. The core holes generated

during XA can be filled (c) by transitions from Mn 3d to Mn 2p orbitals (3d-PFY); (d) by transitions from Mn 3s to Mn 2p orbitals (3s-PFY); or (e) by transitions from O 2p to O 1s orbitals (IPFY). These transitions cause fluorescence emission whose yield is detected. Energetic differences are not to scale.

The absorption of soft X-rays in LSMO generates holes in the core states (Fig. 2a). Three processes are relevant to the discussion herein: (i) the resonant dipole transition of an electron from a Mn $2p^{3/2}$ orbital to a partially filled Mn 3d orbital corresponding to the Mn-L₃ edge; (ii) the resonant dipole transition of an electron from a Mn $2p^{1/2}$ orbital to a partially filled Mn 3d orbital corresponding to the Mn-L₂ edge; and (iii) the non-resonant transition of an electron from an O 1s orbital to an unbound state, i.e. vacuum, which corresponds to XAS above the O-K edge. The transition energies of processes (i) and (ii) differ due to spin-orbit splitting of the 2p orbital with the total angular momentum quantum numbers $j = 3/2$ and $1/2$. Furthermore, the Mn 3d orbitals are hybridized with O 2p,²⁴ which we will not state explicitly unless required for discussion. The electron holes in all three core levels can be filled by various radiative processes where the generated X-ray fluorescence is measured by X-ray emission spectroscopy herein (Fig. 2b-e).

The so-called fluorescence yields (FY) are distinguished by the involved transitions. Without discrimination of the radiate decay channel, i.e. without an X-ray emission spectrometer, the total fluorescence yield (TFY) is obtained. Since each type of detector picks up all possible decay channels (also of all other elements) with different efficiency, it depends on the used detector. Here, we use the Σ -PFY (Fig. 2b), which we define as the sum of the three detected partial fluorescence yields (PFY). This definition excludes noise and artefacts such as “bleeding” from the obtained XAS spectra and was thus used instead of all detected emission energies (compare VLS-TFY and Σ -TFY in Fig. S2). The 3d-PFY is caused by resonant transitions from Mn 3d orbitals to the Mn 2p core holes (Fig. 2c), while the 3s-PFY

is caused by resonant transitions from Mn 3s orbitals also to Mn 2p core holes (Fig. 2d). Thus, both PFY are proportional to the number of created core holes in an ideal case, which makes them also indirect measures of the XA. The fluorescence can also be detected non-resonantly, as is the case when the emission due to the transition from O 2p orbitals to O 1s core holes are probed at excitation energies near the Mn-L_{3,2} edges (Fig. 2e). Achkar and coworkers¹⁷ found that probing this FY shows minima where the 3d-PFY (and also 3s-PFY) has maxima. The inverse partial fluorescence yield (IPFY) can be measured non-resonantly at any emission line below the one of interest, here oxygen, and is thus also an indirect measure of the XA. However, it measures the attenuation length in the probed material rather than created core holes.²⁵

The spectral shape of the Mn-L_{3,2} edges gives valuable insights into the electronic band structure of LSMO but requires elaborate theoretical treatment for quantitative discussion. Here, we discuss the effects qualitatively. In 2p⁶3d⁴ to 2p⁵3d⁵ transitions at the Mn-L_{3,2} edges, the states of two partially filled shells strongly overlap, and thus many body effects have large impact on the spectra. Changes in the electronic band structure of the Mn 3d bands due to spin, spin orbit coupling, doping, ligand symmetry and Mn-O hybridization are reflected in the spectral intensity of the Mn-L_{3,2} edges only indirectly. Some information can be extracted from changes of the L₃/L₂ ratio, where a 2:1 relation is expected from the manifold of the j_m sublevels in a single electron picture.²⁶ However, this ratio is modified due to crystal field splitting and spin orbit coupling of the 3d electrons and depends on the 3dⁿ filling, as described by crystal field multiplet theory.²⁶ The determination of electronic properties of Mn, such as formal valence state, thus requires a careful analysis of the distortion effects due to measurement geometry, energy dependent extinction length, self-absorption of fluorescence radiation and backgrounds from nearby absorption edges.

The Fluorescence Equation and its Low-Absorption Limit

In order to determine the origin of the deviations between the actual XA and PFY spectra, one has to analyze the different excitation processes due to absorption of X-ray photons (Fig. 2a). The relevant energy range is 635-665 eV for the Mn-L_{3,2} edges to see changes of the absorption of Mn 2p electrons. Absorption takes place resonantly at the Mn-L edge but also non-resonantly due to transitions of other elements. Since the fluorescence of the non-resonant transitions can be energetically much lower, here O-K α = 524.9 eV,²⁷ also energies below the Mn-L edge have to be considered as contributing to the background. For XAS in transmission geometry, the intensity of the transmitted X-rays depends on the energy-dependent absorption coefficient $\mu(E)$ and the sample thickness as described by the Beer-Lambert law. In contrast, the degree of absorption is measured indirectly via the fluorescence radiation for PFY measurements (Fig. 2c-e). In this case, the generated fluorescence radiation has to pass different distances through the sample back to the surface before it is emitted from the surface and recorded at the detector. Certainly, the exponential dependency of the Beer-Lambert law also holds for the reabsorption of the fluorescence photons along the length of the emission path out of the sample. Therefore, the resulting Beer-Lambert like law for the emitted fluorescence intensity $I^X(E)$ of the transition of interest X as a function of incident energy E needs to take into account both effects and is given by:¹⁶

$$I^X(E) = \eta \frac{A}{4\pi r^2} \omega_X(E_f, E) \frac{\frac{\mu_X(E)}{\sin \alpha}}{\frac{\mu_{tot}(E)}{\sin \alpha} + \frac{\mu_{tot}(E_f)}{\sin \beta}} \cdot I_0(E) \left[1 - \exp \left(-\frac{d}{\sin \alpha} \mu_{tot}(E) - \frac{d}{\sin \beta} \mu_{tot}(E_f) \right) \right] \quad (1)$$

Here, η is the efficiency of the detector, A the area which was covered by the detector at a distance r and $\omega_X(E_i, E)$ is the fluorescence yield of the transition of interest. α and β are the angles of incidence and detection, respectively, both with respect to the surface (as illustrated in Fig. 1). $I_0(E)$ denotes the incident intensity at energy E , E_f the energy of the fluorescence radiation and d the sample thickness. μ describes the absorption coefficients with $\mu_{tot} = \mu_X + \mu_{BG}$ being the total absorption coefficient. μ_{BG} reflects the background absorption of shallower core levels, valence levels and other atomic species.

For the discussion of this equation, it can be divided into three factors. The first factor, $\eta A / (4\pi r^2) \omega_X(E_f, E)$, describes the fraction of the isotropically emitted fluorescence radiation at a yield $\omega_X(E_f, E)$ which is detected at the solid angle covered by the detector. It assumes an energetically independent characteristic curve $\eta(E) \approx const$ of the detector, as provided by the used grating. Furthermore, the fluorescence yield also changes as function of energy²⁸ but details are unknown for the Mn-L_{3,2} edges. Thus, we treat it to be energy-independent in our simulations. The last factor of the equation, i.e. $I_0(E)$ times the expression in squared brackets, reflects the Beer-Lambert-like penetration of the incident X-ray photons at energy E and angle α , and the emission of the created fluorescence photons at energy E_F and angle β . The modifications of the sample thickness via α and β describe the variation of the optical paths in the sample for the incident and detected fluorescence X-ray radiation, respectively. Since we are interested in the absorption A and can neglect reflections, the degree of absorption is calculated from the transmitted intensity T as $A = 1 - T$.

The middle factor of Eq. (1) reflects the fraction of the absorption of incident photons at the transition of interest, X , to the total absorption of incident and fluorescence photons and weighted over their corresponding lengths of the optical paths in the sample. This can be rewritten as $\frac{\mu_X(E)}{\mu_{tot}(E) + \mu_{tot}(E_f)g}$ with $g = \frac{\sin \alpha}{\sin \beta}$ being a geometric factor. In our experiments, the

detector was mounted perpendicular to the incoming X-rays (Fig. 1). This yields $\alpha + \beta = 90^\circ$. For the case with $\alpha = \beta = 45^\circ$, this results in $g = 1$ (Fig. 3a). For grazing incidence, β almost reaches 90° and thus the length of the optical path for fluorescence radiation is minimal (Fig. 3b). In the limit of $g \rightarrow 0$ (i.e. $\alpha \rightarrow 0^\circ$), the middle factor is $\mu_X(E)/\mu_{tot}(E)$. For simplicity, circular polarized light was used for all experiments in order to avoid further influences of the different orientations of the orbitals involved in the relaxation processes.¹⁸

For the 3s-PFY, we can make a further simplification, namely the assumption that the escape depth of the involved x-ray photons is very small and thus $d \rightarrow 0$. Since only a low fraction of electrons occupy this decay channel, the reabsorption of the 3s fluorescence due to 3s holes is negligible. Therefore, the exponential part of Eq. (1) depending on d can be expressed as a first-order Taylor expansion:

$$\exp\left[-d\left(\frac{\mu_{tot}(E)}{\sin\alpha} + \frac{\mu_{tot}(E_f)}{\sin\beta}\right)\right] \approx 1 - \left(\frac{\mu_{tot}(E)}{\sin\alpha} + \frac{\mu_{tot}(E_f)}{\sin\beta}\right)d. \quad (2)$$

This simplifies the fluorescence formula of the 3s-PFY to:

$$I^X(E) \approx \eta \frac{A}{4\pi r^2} \omega_X(E_f) I_0(E) \frac{\mu_X(E)}{\sin\alpha}, \quad (3)$$

which is commonly known as the “thin sample” approximation.²⁹ The remaining angular dependence is linear in $1/(\sin\alpha)$, which is canceled out by the used normalization procedure (details in Experimental section). The resulting normalized spectrum represents the undistorted $\mu_X(E)$.

Simulated Fluorescence Yields

Figure 3 presents the results of simulations of equations (1) and (3), in order to understand and classify the general trends in distortions of the $L_{3,2}$ PFY spectra. Details of the simulations can be found in Table S1 and Fig. S3. Figure 3c shows the simulated spectral changes of the 3d-PFY as a function of the incident angle α based on Eq. (1). When the angle is lowered, the

L_3 and L_2 peak amplitudes and the intensity between the peaks are both lowered. Yet, we note that the L_2 edge step was set to zero in all calculations, which means that angles near 90° actually lead to an increase in intensity between the L_3 and L_2 peaks. The ratio of the intensities at the L_3 to the L_2 peak was set to 2.14 for the actual XA spectrum and it decreases in the simulations from 2.08 at 89° to 1.60 at 45° to 1.25 at 1° (Table S2). No changes with the angle ($L_3/L_2 = 2.14$) are visible for the normalized 3s-PFY (Fig. 3e) as expected from Eq. (3) and the discussion above. For the IPFY (Fig. 3g), a different behavior can be seen in simulations based on Eq. (1). First, the intensities increase with decreasing the angle from 89° to 20° and then they decrease again for lower angles (Table S2). Consequently, the L_3/L_2 ratio increases from 0.92 at 89° to 2.12 at 20° and slightly decreases to 2.03 at 1° (Table S2). These changes may be attributed to the normalization procedure (Experimental section and Fig. S1).

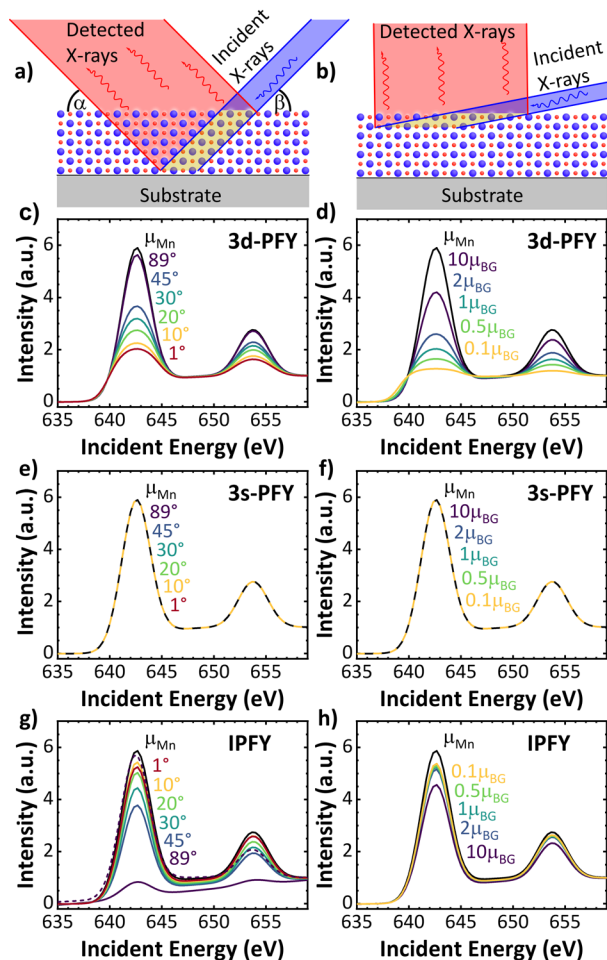


Figure 3. Schematic visualization of the change in measurement geometry from (a) bulk penetration to (b) grazing incidence for LSMO on a substrate (not to scale). The XAS at the Mn-L_{3,2} edges was simulated for (c,d) the 3d-PFY, (e,f) the 3s-PFY, and (g,h) the IPFY as a function of the angle of incidence α (left column) and as a function of background absorption for $\alpha = 1^\circ$ (right column). The absorption coefficient μ_{Mn} (black lines) was constructed by adding two Gaussians to the absorption data from the Henke tables² (Fig. S3). The dashed lines in panels e and f were chosen to show that all curves overlap. All spectra were normalized as detailed the Experimental part with the exception of the dotted line in panel g where a linear function rather than averages were used (see text for detail). The sum of the angles $\alpha + \beta$ was fixed at 90° in all simulations. The color codes are here equally for c, e and g, as well as d, f, and h, respectively. Simulation parameters are described in Table S1 and Fig. S3.

The main reason for the strong angular dependence of the 3d-PFY is a strong angular dependence of the escape depth l_f of the generated fluorescence photon with $l_f * \sin \alpha$, where l_f for LSMO at the Mn -L edge is about 230 nm based on the Henke tables.² A decreased escape depth for the fluorescence results in a shorter optical path in the sample towards the detector and thus a decreased degree of reabsorption. This leads to strong distortions for E_f , where $\mu_{\text{tot}}(E_f)$ is relatively large and strongly influenced by the experimental angles. In Fig. 3c, the spectra for decreasing α (violet to red) thus appear more saturated.

In addition to the angle-dependent distortion, deviations from the actual XA spectrum may arise due to the background absorption μ_{BG} from shallower core levels, valence levels and other atomic species. In order to analyze this effect, Mn-L_{3,2} spectra with different degrees of background absorption were simulated (Fig. 3d,f,h). Here, the incidence angle α is kept at 1° for all spectra. For the 3d-PFY (Fig. 3d) the spectral changes upon varying μ_{BG} from weak to strong background absorption are significant. The intensities decrease with lower background absorption. Also, the edge position (energy at 0.5 a.u) shifts from $10\mu_{\text{BG}}$ to $0.1\mu_{\text{BG}}$ by about 0.8 eV towards lower energies. The L₃/L₂ ratio decreases from 1.77 at $10\mu_{\text{BG}}$ to 1.06 at $0.1\mu_{\text{BG}}$

(Table S2). For the 3s-PFY (Fig. 3f) no changes are visible since it does not depend on the background absorption (Eq. 2). The IPFY (Fig. 3h) only shows negligible changes between $0.1\mu\text{BG}$ and $5\mu\text{BG}$ (L_3/L_2 ratio of 2.03 ± 0.01) and slightly decreases at $10\mu\text{BG}$ to 1.96 (Table S2) due to the normalization procedure.

RESULTS AND DISCUSSION

The experimental verification of the simulated trends requires sufficient emission energy resolution of the recorded RIXS map to distinguish the spectral features. Figure 4 shows a typical RIXS map of the Mn-L edge of the 80 nm thick LSMO film. It was recorded at an incident angle of $\alpha = 45^\circ$ and detection angle of $\beta = 45^\circ$ (Definition of angles in Fig. 1). The RIXS map was generated from X-ray emission at different incident energies around the Mn-L edge in steps of 0.2 eV as described in the experimental section.

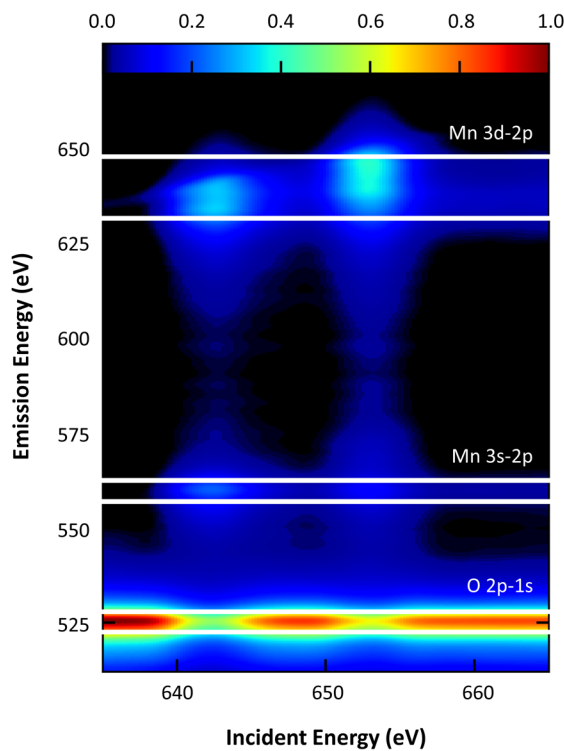


Figure 4. RIXS map of the LSMO thin film excited along the Mn-L edge for $\alpha = 45^\circ$ showing all three relevant transitions marked by white boxes. The intensities are color-coded and were normalized between 1 and 0 (top scale). The data was smoothed via a Gaussian filter with $\sigma = 4$ for clarity. The original RIXS map can be found in Fig. S4.

Although the recorded RIXS map contains richer information, the focus of this work is on the analysis of the different PFY channels. We start with the analysis of three emission lines that can be resolved individually, namely the Mn 3d-2p, the Mn 3s-2p and the O 2p-1s transitions. Appropriate regions of interest (ROI) are defined through FWHM of the XES (white boxes in Fig. 4). Although the Mn 3s-2p emission is about 13 times less intense than the Mn 3d-2p emission,²⁷ it was acquired with a signal to noise ratio and energy resolution comparable to the Mn 3d-2p transition. Vertical integration of the ROIs and representation over the incident energy allows the generation of the corresponding PFY spectra. The Σ -PFY, as defined and discussed above, is calculated as the sum of the three ROIs in Fig. 4.

The extracted PFY spectra in Fig. 4 differ from the simulated multiplet features of the X-ray absorption spectra at 45° , where an L_3/L_2 ratio of about 2.4 is expected for Mn^{3+} and 1.6 for Mn^{4+} .²⁶ The observed ratio decreases from the 3s-PFY (1.96), to the IPFY (1.27), to the 3d-PFY (0.72), to the Σ -PFY (0.65). These deviations were also previously discussed in literature.^{16,25} Even though the IPFY (turquoise) and the 3s-PFY (green) both were claimed to give bulk spectra, which are free of distortions,^{17,18} their intensities differ significantly at the L_3 edge. Due to the limited energy range before the L_3 edge, it was not possible to use a polynomial background for the IPFY and thus the intensity ratio is additionally influenced by the normalization procedure (Fig. S3). The L_3 intensities of the IPFY are also reduced since the primary contributions to μ_{BG} stem from heavy atoms (La-N and Sr-M edges) with much higher photoabsorption cross sections.²

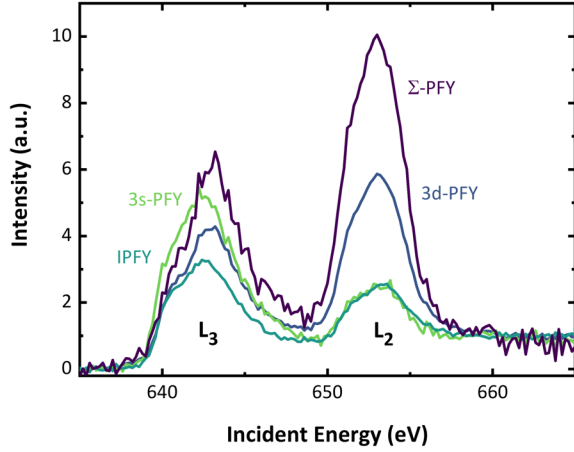


Figure 5. PFY spectra of LSMO at the Mn-L edges for $\alpha = 45^\circ$. Distortions of the spectra are most pronounced in the order of increasing L_3/L_2 intensity ratio, i.e. Σ -PFY (violet), 3d-PFY (blue), IPFY (turquoise) and 3s-PFY (green).

Figure 6 shows the different PFY spectra at 45° and 1° incident angle in comparison to the angular dependence from models based on optimized simulations of Eq. (1) and its limiting case in Eq. (3). The corresponding RIXS maps may be found in Fig. S5. Fits to the 45° spectra were carried out by modelling the edge jump as arctangent functions and the multiplet structure of the L_3 and L_2 edges as two Gaussians (Fig. S3a). These obtained parameters were used to determine μ_{Mn} , from which we simulated the spectra at grazing incidence, i.e. at 1° , using Eqs. (1) or (3). Details of the simulations can be found in Table S3.

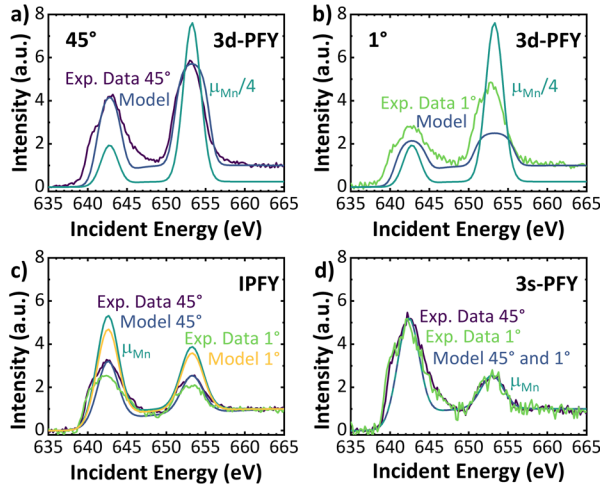


Figure 6. (a) Comparison of experimental 3d-PFY at an incident angles $\alpha = 45^\circ$ (purple line) and model (blue line) together with the undistorted μ_{Mn} (turquoise line). (b) The same for $\alpha = 1^\circ$ with the same model parameters varied only by the experimental angles in the fluorescence formula. (c) Experimental data for the IPFY (violet and green) with their corresponding models (blue and yellow) and μ_{BG} (turquoise). (d) Experimental data for the 3s-PFY for $\alpha = 45^\circ$ (violet) and $\alpha = 1^\circ$ (green) with the true absorption spectrum (turquoise) and the identical models (blue). Additional details about the models may be found in Table S3.

The 3d-PFY for $\alpha = 45^\circ$ in Fig. 6a deviates from an ideal undistorted μ_{Mn} (turquoise). Furthermore, using $\mu_{Mn}(45^\circ)$ for simulating the variations from $\alpha = 45^\circ$ to 1° according to eq. (1) in Fig. 6a,b correctly predicts a reduction of the amplitudes but does not match the experimentally observed peak heights (Table S4). Some deviations may be due to the energy dependence of the fluorescence yield $\omega_x(E_f, E)^{28}$ that was not included in the model. The measured intensities at $\alpha = 1^\circ$ are higher than the simulated ones because the degree of absorption of s- and p-polarized X-rays depends on the incident angle.^{30,31} The results show that the 3d-PFY underlies distortions due to strong angular dependence, which cannot be described by the fluorescence formula. The L_3 edge of the Σ -PFY is not further considered due to the strong distortions from its ill-defined background³² and particularly the drastically

reduced L₃ edge at 1° (Fig. S2b). Consequently, both Σ -PFY and the 3d-PFY are not suitable for the analysis of surface processes.

For the IPFY (Fig. 6c), small deviations occur at 45°, particularly after the L₃ edge. This is due to the fact that the complex multiplet structure of each edge is assumed here as a single Gaussian, which is a strong simplification not accounting for the L₂ edge jump in the model. While the model for 45° (blue) is in a good agreement with the experimental data (violet), varying only the experimental angles towards $\alpha = 1^\circ$ with all other parameters fixed (yellow) cannot reproduce the experimental data recorded at that angle (green). The experimental intensities are strongly decreased relative to the other fluorescence yields at both edges due to the normalization procedure. The experimental L₃/L₂ ratio changes from $\alpha = 45^\circ$ to 1° from 1.27 to 1.22, respectively. An edge shift of -0.2 eV occurs.

The 3s-PFY (Fig. 6d) shows no angular dependency in the experimental spectra in accordance to the simulated spectra as described above. The model of the absorption spectrum of Mn, μ_{Mn} , (turquoise) is in a good agreement with the experimental data for 45° (violet) and for 1° (green). The L₃/L₂ ratio of the 3s-PFY was identical to that of μ_{Mn} , i.e. 2.15, after normalization. The 3s-PFY thus directly reflects the profile of generated 2p holes below the sample surface and is a good proxy of an XA spectrum. Also, Miedema et al.¹⁸ modelled 3s-PFY spectra for the transition metals Ti, Fe and Ni, which showed undistorted XA spectra. Since they simulated linearly polarized X-rays, distortion-free spectra were only observed at the magic angle of 54.7°, where all polarization directions contribute equally. At this angle, their result is thus comparable to our study where circularly polarized X-rays were used, for which all directions also contribute equally. Indeed, the 3s-PFY is not affected by the polarization angle, due to the spherical symmetry of the 3s orbital. Since the 3s-PFY is also not distorted by angle-dependent background variations due to other elements such as oxygen concentration changes at surfaces, it is the most suitable PFY for surface sensitive Mn-L edge

X-ray spectroscopy studies. There is an edge shift of -0.2 eV at the L₃ edge, similar to the IPFY. Interestingly, the edge shift is not visible in the L₂ edge of the 3s-PFY (Fig. S7h). This may be due to different lifetime broadening of 1.5 eV for the L₂ edge, which is much stronger than the 0.4 eV broadening for the L₃ edge.³³

LSMO surfaces and subsurface can differ from bulk properties due to two main effects: (i) Surface reconstruction due to a change Mn-O coordination or octahedral tilting which can affect the crystal field splitting as well as Mn-O charge transfer;³⁴ and (ii) surface reconstruction due to the presence of surface or subsurface oxygen vacancies.³⁵ Typically, a shift in XAS towards lower energies is attributed to a reduced state.^{35,36} Since the spectra recorded at $\alpha = 1^\circ$ probed only about 10 unit cells of the sample, the observed edge shift in the IPFY and 3s-PFY may be a hint for a reduced surface and subsurface of the LSMO film compared to the bulk. Since with the IPFY effectively the penetration depth is probed,²⁵ the reduced intensities under grazing incidence show a reduced oxygen content in the probed volume. The edge shift of the IPFY to lower energies from 45° to 1° could either be assigned to Mn reduction based on reference materials³⁶ or to changes in crystal field splitting and charge transfer.³⁷ From our simulations, an artefact due to angular dependence or background-dependent distortions of the spectra (Fig. 3g,h) is improbable.

Figures 7 and S6 compare Σ -PFY, 3d-PFY, IPFY and 3s-PFY for an incident angle of $\alpha = 1^\circ$ (blue) without and with water. An additional water layer does not change the 3d-PFY (Fig. 7a) and the IPFY (Fig. 7b) but is visible in significant changes in the grazing incidence 3s-PFY data (Fig. 7c). In the 3d-PFY, the change of $\mu_{BG}(E)$ by the additional water layer might be negligible, because of the large signal to noise ratio. Since the IPFY is non-resonantly representing a Mn-L edge spectrum, additional water at the surface only gives rise to an additional O 1s emission of the oxygen in water. This leads to an energy-independent change of the IPFY over the whole energy range and is thus invisible after the normalization of the

data. Since the 3s-PFY does not show distortions due to angular-dependent background changes as mentioned above, it is the most suitable PFY for surface sensitive Mn-L edge X-ray spectroscopy studies.

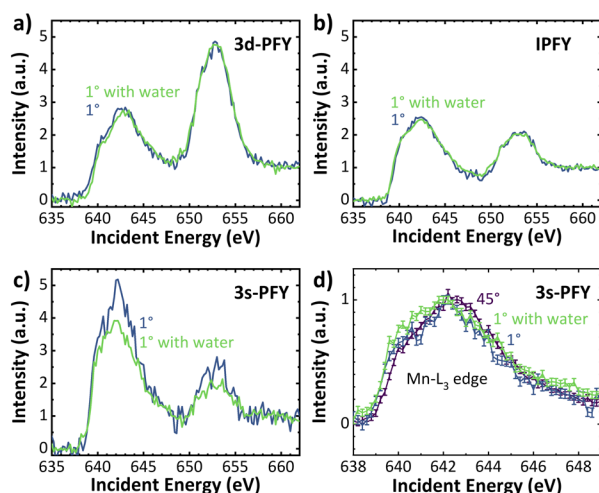


Figure 7. Comparison of the experimental XAS with water vapor (turquoise) and without water vapor (blue) at grazing incidence of 1° for (a) the 3d-PFY, (b) the IPFY and (c) the 3s-PFY. (d) the Mn-L₃ edge in the 3s-PFY mode normalized to the maximum of the Mn-L₃ edge.

We argue in the following that the changes of the 3s-PFY in Figs. 7c,d due to water at the surface gives access to water-induced changes in surface electronic states of the LSMO. First of all, the strong decrease of the overall 3s-PFY intensity in water may be attributed to a stronger absorption of the surface fluorescence by the water layer (Fig. 7c). After normalizing the 3s-PFY spectra to the L₃ edge maximum in Fig. 7d, even more pronounced features can be seen. We focus on the L₃ edge since the changes are more distinct due to the smaller lifetime broadening as discussed above. The low energy shoulder formed at 640 eV for $\alpha = 1^\circ$ in vacuum is further changed in water. One possible explanation of its increase in intensity in the energy range between 640 and 642 eV may be a further surface reduction in water. However, there is an additional small pre-peak at about 638 eV and a satellite feature at 647.5 eV. These

additional features point to other effects than surface reduction, which change the L_3 3s-PFY spectra in water. A broadening is discussed in terms of a decrease of the crystal field splitting ($10 Dq$)³⁸ as well as it can be a fingerprint for an increased ligand to metal charge transfer (LMCT).²⁶ Furthermore, the satellite feature at higher energies is supportive for a LMCT.³⁹ A decrease of the crystal field splitting is expected at the LSMO surface due to the change from a pure octahedral coordination with point group O_h towards a more spherical coordination.^{26,39} Indeed, this symmetry reduction is heavily influenced by chemisorbed water, even more if it induces structural surface disorder. A change in MnO_6 symmetry and changes in LMCT are of course strongly interdependent due to the involved changes in overlap between Mn 3d and O 2p orbitals.

Comparing our results for changes of the LSMO surface in water with literature, the experimental evidence for an increase in surface reduction of Mn is rather scarce. A careful study of the same LSMO (001) films before and after oxygen evolution via XPS does not find any indication for oxygen vacancy formation.⁵ Despite gradual leaching of Sr and Mn in the active state of the surface at an applied potential, the surface oxygen concentration remained constant. Cyclovoltammetry at pH = 13 does not show any surface redox peak in LSMO indicating Mn surface reduction, as observed in other manganites (e.g. in ref. 40). Post-mortem transmission electron microscopy (ETEM) studies of the LSMO (001) surface after electrochemical water oxidation show a stable LSMO surface and no sign of Mn reduction.¹² This observation clearly supports the hypothesis of Mn-O bond changes affecting ligand field splitting and charge transfer, visible in the 3s-PFY and points against the interpretation of surface reduction.

The presented indirect XAS study of a LSMO (001) surface demonstrates that it is possible to study surface processes, also under *in situ* conditions by grazing incidence XAS using a highly resolving RIXS spectrometer. The observed IPFY and the 3s-PFY edges shift towards

lower energies for proceeding from bulk to surface sensitive measurement geometry is consistent with a reduced surface state of the pristine LSMO (001) film due to surface oxygen vacancies, since satellite features in 3s-PFY are absent. For measurements with an additional water layer, only the 3s-PFY shows significant changes, since the IPFY only monitors an energy independent background from water oxygen. In contrast, the features in 3s-PFY suggest the change in Mn ligand bonding due to the presence of water on the LSMO surface, consistent with the observation of disordered surface Mn, due to partial solvation. Therefore, we emphasize the improvement of soft X-ray spectrometers, especially considering the capability of recording separated and highly resolved IPFY and 3s-PFY for *in situ* studies.

CONCLUSION

We studied the differences of four soft PFY techniques with respect to surface-sensitivity and under *in situ* conditions at the Mn-L edge of a model catalyst. The spectra of the 3d-PFY, IPFY and 3s-PFY under *ex situ* conditions are well simulated, using the fluorescence formulas in Eqs. (1) and (3). All PFY methods are capable of resolving surface-sensitivity when changing the incident photons to grazing incidence, even though the changes were most pronounced for the IPFY and 3s-PFY. Moreover, only the 3s-PFY is independent of the polarization angle due to the spherical symmetry of the 3s orbital. Thus, the 3s-PFY is most capable of resolving surface processes under *in situ* conditions. In contrast, the Σ -PFY and the 3d-PFY heavily suffer from distortions due to energy dependent self-absorption of the fluorescence radiation leading to an increased background. The IPFY yields surface sensitive electronic information but is less suitable for *in situ* studies since it also probes the water oxygen as a constant background contribution. The analysis of 3s-PFY in grazing incidence geometry without and with water gives access in changes of surface electronic states of Mn atoms and their bonding to oxygen.

Our data gives strong evidence for changes in ligand symmetry and charge transfer to oxygen atoms in water due to water surface adsorption. Our work thus demonstrates the feasibility of *in situ* 3s-PFY to probe surface processes, which is crucial for, e.g., corrosion or catalysis.

AUTHOR INFORMATION

Corresponding Authors

[*marcel.risch@helmholtz-berlin.de](mailto:marcel.risch@helmholtz-berlin.de)

(ORCID: 0000-0003-2820-7006)

Tel: +49 (0)30 806242609

[*simone.techert@desy.de](mailto:simone.techert@desy.de)

(ORCID: 0000-0002-7549-7651)

Tel: +49 (0) 40 8998 4880

[*cjooss@gwdg.de](mailto:cjooss@gwdg.de)

(ORCID: 0000-0002-8762-9359)

Tel: +49 (0)551 3925303

Present Addresses

*†Laboratory of Physical Chemistry, Eidgenössische Technische Hochschule Zürich, 8093
Switzerland*

*††Helmholtz Centre Berlin for Materials and Energy GmbH, Department Optics and
Beamlines (NP-AOS), 12489 Berlin, Germany*

ACKNOWLEDGEMENT

Funding by the Deutsche Forschungsgemeinschaft (DFG) via the CRC 1073 “Atomic scale control of energy conversion”, projects B06 (#217133147), C01 (#217133147), C02 (#217133147) and C05 (#217133147) are gratefully acknowledged. S.T. is grateful to CRC 755 “Nanoscale Photonic Imaging”, project B03 (#28586557). We acknowledge DESY (Hamburg, Germany), a member of the Helmholtz Association HGF, for the provision of experimental facilities. Parts of this research were carried out at PETRA III on proposal I-20160079 and we would like to thank the beamline scientists of beamline P04 as well as Sascha Deinert (DESY) and Emanuel Ronge (University of Goettingen) for their support during the measurements. The research has financially been supported by the Max Planck Society (MPIbpC) and the Helmholtz Association.

SUPPORTING INFORMATION

Illustration of the normalization procedure, additional PFY spectra and RIXS maps, construction of μMn , parameters and formulas used in the simulations and fits.

REFERENCES

- (1) de Groot, F. High-Resolution X-Ray Emission and X-Ray Absorption Spectroscopy. *Chem. Rev.* **2001**, *101* (6), 1779–1808.
- (2) Henke, B. L.; Gullikson, E. M.; Davis, J. C. X-Ray Interactions: Photoabsorption, Scattering, Transmission, and Reflection at $E = 50\text{--}30,000$ EV, $Z = 1\text{--}92$. *At. Data Nucl. Data Tables* **1993**, *54* (2), 181–342. <https://doi.org/10.1006/ADND.1993.1013>.
- (3) Risch, M. Perovskite Electrocatalysts for the Oxygen Reduction Reaction in Alkaline Media. *Catalysts* **2017**, *7* (5), 154. <https://doi.org/10.3390/CATAL7050154>.
- (4) Hong, W. T.; Risch, M.; Stoerzinger, K. A.; Grimaud, A.; Suntivich, J.; Shao-Horn, Y. Toward the Rational Design of Non-Precious Transition Metal Oxides for Oxygen Electrocatalysis. *Energy Environ. Sci.* **2015**, *8* (5), 1404–1427. <https://doi.org/10.1039/C4EE03869J>.
- (5) Scholz, J.; Risch, M.; Stoerzinger, K. A.; Wartner, G.; Shao-Horn, Y.; Jooss, C. Rotating Ring-Disk Electrode Study of Oxygen Evolution at a Perovskite Surface: Correlating Activity to Manganese Concentration. *J. Phys. Chem. C* **2016**, *120* (49), 27746–27756. <https://doi.org/10.1021/acs.jpcc.6b07654>.
- (6) Kotani, A.; Shin, S. Resonant Inelastic X-Ray Scattering Spectra for Electrons in Solids. *Rev. Mod. Phys.* **2001**, *73* (1), 203–246. <https://doi.org/10.1103/RevModPhys.73.203>.
- (7) Ament, L. J. P.; van Veenendaal, M.; Devereaux, T. P.; Hill, J. P.; van den Brink, J. Resonant Inelastic X-Ray Scattering Studies of Elementary Excitations. *Rev. Mod. Phys.* **2011**, *83* (2), 705–767. <https://doi.org/10.1103/RevModPhys.83.705>.

- (8) Yin, Z.; Rajkovic, I.; Veedu, S. T.; Deinert, S.; Raiser, D.; Jain, R.; Fukuzawa, H.; Wada, S.-I.; Quevedo, W.; Kennedy, B.; et al. Ionic Solutions Probed by Resonant Inelastic X-Ray Scattering. *Z. Phys. Chem* **2015**, *229*, 1855–1867. <https://doi.org/10.1515/zpch-2015-0610>.
- (9) Soldatov, M. A.; Lange, K. M.; Gotz, M. D.; Engel, N.; Golnak, R.; Kothe, A.; Aziz, E. F. On the Origin of Dips in Total Fluorescence Yield X-Ray Absorption Spectra: Partial and Inverse Partial Fluorescence Yield at the L-Edge of Cobalt Aqueous Solution. *Chem. Phys. Lett.* **2012**, *546*, 164–167. <https://doi.org/10.1016/j.cplett.2012.07.067>.
- (10) de Groot, F.; Kotani, A. *Core Level Spectroscopy of Solids*; Advances in Condensed Matter Science; CRC Press, 2008; Vol. 6. <https://doi.org/10.1201/9781420008425>.
- (11) Favaro, M.; Jeong, B.; Ross, P. N.; Yano, J.; Hussain, Z.; Liu, Z.; Crumlin, E. J. Unravelling the Electrochemical Double Layer by Direct Probing of the Solid/Liquid Interface. *Nat. Commun.* **2016**, *7*, 12695. <https://doi.org/10.1038/ncomms12695>.
- (12) Scholz, J.; Risch, M.; Wartner, G.; Luderer, C.; Roddatis, V.; Jooss, C. Tailoring the Oxygen Evolution Activity and Stability Using Defect Chemistry. *Catalysts* **2017**, *7* (5), 139. <https://doi.org/10.3390/catal7050139>.
- (13) Kawasaki, M.; Izumi, M.; Konishi, Y.; Manako, T.; Tokura, Y. Perfect Epitaxy of Perovskite Manganite for Oxide Spin-Electronics. *Mater. Sci. Eng. B* **1999**, *63* (1), 49–57. [https://doi.org/10.1016/S0921-5107\(99\)00051-3](https://doi.org/10.1016/S0921-5107(99)00051-3).
- (14) Jaklevic, J.; Kirby, J. A.; Klein, M. P.; Robertson, A. S.; Brown, G. S.; Eisenberger, P. Fluorescence Detection of EXAFS: Sensitivity Enhancement for Dilute Species and Thin Films. *Solid State Commun.* **1977**, *23* (9), 679–682. <https://doi.org/10.1016/0038->

1098(77)90548-8.

- (15) Risch, M.; Stoerzinger, K. A.; Regier, T. Z.; Peak, D.; Sayed, S. Y.; Shao-Horn, Y. Reversibility of Ferri-/Ferrocyanide Redox during Operando Soft X-Ray Spectroscopy. *J. Phys. Chem. C* **2015**, *119* (33), 18903–18910. <https://doi.org/10.1021/acs.jpcc.5b04609>.
- (16) Eisebitt, S.; Böske, T.; Rubensson, J.-E.; Eberhardt, W. Determination of Absorption Coefficients for Concentrated Samples by Fluorescence Detection. *Phys. Rev. B* **1993**, *47* (21), 14103–14109. <https://doi.org/10.1103/PhysRevB.47.14103>.
- (17) Achkar, A. J.; Regier, T. Z.; Wadati, H.; Kim, Y.-J.; Zhang, H.; Hawthorn, D. G. Bulk Sensitive X-Ray Absorption Spectroscopy Free of Self-Absorption Effects. *Phys. Rev. B* **2011**, *83* (8), 081106. <https://doi.org/10.1103/PhysRevB.83.081106>.
- (18) Miedema, P. S.; Beye, M. Total 3s Emission Yield as Bulk-Sensitive Probe for a True Soft X-Ray Absorption Spectrum? *J. Phys. Chem. Lett.* **2018**, *9* (10), 2579–2583. <https://doi.org/10.1021/acs.jpcllett.8b00720>.
- (19) Golnak, R.; Xiao, J.; Atak, K.; Unger, I.; Seidel, R.; Winter, B.; Aziz, E. F. Undistorted X-Ray Absorption Spectroscopy Using s-Core-Orbital Emissions. *J. Phys. Chem. A* **2016**, *120* (18), 2808–2814. <https://doi.org/10.1021/acs.jpca.6b01699>.
- (20) Galakhov, V. R.; Demeter, M.; Bartkowski, S.; Neumann, M.; Ovechkina, N. A.; Kurmaev, E. Z.; Lobachevskaya, N. I.; Mukovskii, Y. M.; Mitchell, J.; Ederer, D. L. Mn Exchange Splitting in Mixed-Valence Manganites. *Phys. Rev. B* **2002**, *65* (11), 113102. <https://doi.org/10.1103/PhysRevB.65.113102>.
- (21) Viefhaus, J.; Scholz, F.; Deinert, S.; Glaser, L.; Ilchen, M.; Seltmann, J.; Walter, P. The

- Variable Polarization XUV Beamline P04 at PETRA III: Optics, Mechanics and Their Performance. *Nucl. Instruments Methods Phys. Res. Sect. A Accel. Spectrometers, Detect. Assoc. Equip.* **2013**, *710*, 151–154. <https://doi.org/10.1016/J.NIMA.2012.10.110>.
- (22) Yin, Z.; Peters, H. B.; Hahn, U.; Agåker, M.; Hage, A.; Reiningner, R.; Siewert, F.; Nordgren, J.; Viefhaus, J.; Techert, S. A New Compact Soft X-Ray Spectrometer for Resonant Inelastic x-Ray Scattering Studies at PETRA III. *Rev. Sci. Instrum.* **2015**, *86* (9), 093109. <https://doi.org/10.1063/1.4930968>.
- (23) Yin, Z.; Peters, H.-B.; Hahn, U.; Gonschior, J.; Mierwaldt, D.; Rajkovic, I.; Viefhaus, J.; Jooss, C.; Techert, S.; An Endstation for Resonant Inelastic X-Ray Scattering Studies of Solid and Liquid Samples. *J. Synchrotron Radiat.* **2017**, *24* (1), 302–306. <https://doi.org/10.1107/S1600577516016611>.
- (24) Ebrahimizadeh Abrishami, M.; Risch, M.; Scholz, J.; Roddatis, V.; Osterthun, N.; Jooss, C. Oxygen Evolution at Manganite Perovskite Ruddlesden-Popper Type Particles: Trends of Activity on Structure, Valence and Covalence. *Materials* **2016**, *9* (12), 921. <https://doi.org/10.3390/ma9110921>.
- (25) Achkar, A. J.; Regier, T. Z.; Monkman, E. J.; Shen, K. M.; Hawthorn, D. G. Determination of Total X-Ray Absorption Coefficient Using Non-Resonant X-Ray Emission. *Sci. Rep.* **2011**, *1*, 182. <https://doi.org/10.1038/srep00182>.
- (26) Groot, F. de. Multiplet Effects in X-Ray Spectroscopy. *Coord. Chem. Rev.* **2005**, *249* (1–2), 31–63. <https://doi.org/10.1016/j.ccr.2004.03.018>.
- (27) Bearden, J. A. X-Ray Wavelengths. *Rev. Mod. Phys.* **1967**, *39* (1), 78. <https://doi.org/10.1103/RevModPhys.39.78>.

- (28) Kurian, R.; Kunnus, K.; Wernet, P.; Butorin, S. M.; Glatzel, P.; de Groot, F. M. F. Intrinsic Deviations in Fluorescence Yield Detected X-Ray Absorption Spectroscopy: The Case of the Transition Metal L_{2,3} Edges. *J. Phys. Condens. Matter* **2012**, *24* (45), 452201. <https://doi.org/10.1088/0953-8984/24/45/452201>.
- (29) Newville, M. Fundamentals of XAFS. *Rev. Mineral. Geochemistry* **2014**, *78* (1), 33–74. <https://doi.org/10.2138/rmg.2014.78.2>.
- (30) Schäfers, F.; Mertins, H.-C.; Gaupp, A.; Gudat, W.; Mertin, M.; Packe, I.; Schmolla, F.; Di Fonzo, S.; Soullié, G.; Jark, W.; et al. Soft-x-Ray Polarimeter with Multilayer Optics: Complete Analysis of the Polarization State of Light. *Appl. Opt.* **1999**, *38* (19), 4074. <https://doi.org/10.1364/AO.38.004074>.
- (31) Van Veenendaal, M. Polarization Dependence of L- and M-Edge Resonant Inelastic X-Ray Scattering in Transition-Metal Compounds. *Phys. Rev. Lett.* **2006**, *96* (11), 117404. <https://doi.org/10.1103/PhysRevLett.96.117404>.
- (32) de Groot, F. M. F. Dips and Peaks in Fluorescence Yield X-Ray Absorption Are Due to State-Dependent Decay. *Nat. Chem.* **2012**, *4* (10), 766–767. <https://doi.org/10.1038/nchem.1431>.
- (33) Ravel, B.; Newville, M. ATHENA, ARTEMIS, HEPHAESTUS: Data Analysis for X-Ray Absorption Spectroscopy Using IFEFFIT. *J. Synchrotron Radiat.* **2005**, *12* (4), 537–541. <https://doi.org/10.1107/S0909049505012719>.
- (34) Cui, B.; Song, C.; Li, F.; Wang, G. Y.; Mao, H. J.; Peng, J. J.; Zeng, F.; Pan, F. Tuning the Entanglement between Orbital Reconstruction and Charge Transfer at a Film Surface. *Sci. Rep.* **2014**, *4*, 4206. <https://doi.org/10.1038/srep04206>.

- (35) de Jong, M. P.; Bergenti, I.; Dediu, V. A.; Fahlman, M.; Marsi, M.; Taliani, C. Evidence for Mn²⁺ Ions at Surfaces of La_{0.7}Sr_{0.3}MnO₃ Thin Films. *Phys. Rev. B* **2005**, *71* (1), 014434. <https://doi.org/10.1103/PhysRevB.71.014434>.
- (36) Risch, M.; Stoerzinger, K. A.; Han, B.; Regier, T. Z.; Peak, D.; Sayed, S. Y.; Wei, C.; Xu, Z. J.; Shao-Horn, Y. Redox Processes of Manganese Oxide in Catalyzing Oxygen Evolution and Reduction: An In Situ Soft X-Ray Absorption Spectroscopy Study. *J. Phys. Chem. C* **2017**, *121* (33), 17682–17692. <https://doi.org/10.1021/acs.jpcc.7b05592>.
- (37) de Groot, F.; Fuggle, J.; Thole, B.; Sawatzky, G. 2p X-Ray Absorption of 3d Transition-Metal Compounds: An Atomic Multiplet Description Including the Crystal Field. *Phys. Rev. B* **1990**, *42* (9), 5459–5468. <https://doi.org/10.1103/PhysRevB.42.5459>.
- (38) *Molecular Electronic Structures of Transition Metal Complexes II*; Mingos, D. M. P., Day, P., Dahl, J. P., Eds.; Structure and Bonding; Springer Berlin Heidelberg: Berlin, Heidelberg, 2012; Vol. 143. <https://doi.org/10.1007/978-3-642-27378-0>.
- (39) de Groot, F. M. F. X-Ray Absorption and Dichroism of Transition Metals and Their Compounds. *J. Electron Spectros. Relat. Phenomena* **1994**, *67* (4), 529–622. [https://doi.org/10.1016/0368-2048\(93\)02041-J](https://doi.org/10.1016/0368-2048(93)02041-J).
- (40) Mildner, S.; Beleggia, M.; Mierwaldt, D.; Hansen, T. W.; Wagner, J. B.; Yazdi, S.; Kasama, T.; Ciston, J.; Zhu, Y.; Jooss, C. Environmental TEM Study of Electron Beam Induced Electrochemistry of Pr_{0.64}Ca_{0.36}MnO₃ Catalysts for Oxygen Evolution. *J. Phys. Chem. C* **2015**, *119* (10), 5301–5310. <https://doi.org/10.1021/jp511628c>.

TOC Graphic

